AIP | Journal of Applied Physics

Effects of Au layer thickness and number of bilayers on the properties of Au/ZnO multilayers

Eva Céspedes, David Babonneau, Domingos de Sousa Meneses, Carlos Prieto, Emiliano Fonda et al.

Citation: J. Appl. Phys. **109**, 094308 (2011); doi: 10.1063/1.3580333
View online: http://dx.doi.org/10.1063/1.3580333
View Table of Contents: http://jap.aip.org/resource/1/JAPIAU/v109/i9
Published by the American Institute of Physics.

Additional information on J. Appl. Phys.

Journal Homepage: http://jap.aip.org/
Journal Information: http://jap.aip.org/about/about_the_journal
Top downloads: http://jap.aip.org/features/most_downloaded
Information for Authors: http://jap.aip.org/authors

ADVERTISEMENT

Downloaded 03 May 2013 to 150.244.101.204. This article is copyrighted as indicated in the abstract. Reuse of AIP content is subject to the terms at: http://jap.aip.org/about/rights_and_permissions

JOURNAL OF APPLIED PHYSICS **109**, 094308 (2011)

Effects of Au layer thickness and number of bilayers on the properties of Au/ZnO multilayers

Eva Céspedes,[1] David Babonneau,[2] Domingos de Sousa Meneses,[3] Carlos Prieto,[1] Emiliano Fonda,[4] Olivier Lyon,[4] Emrick Briand,[5] and Agnès Traverse[6,a)]
[1]*Instituto de Ciencia de Materiales de Madrid, CSIC, Cantoblanco, Madrid, 28049, Spain*
[2]*Institut Prime, UPR 3346 CNRS, Université de Poitiers, Boulevard M. et P. Curie, F-86962 Futuroscope, France*
[3]*Centre Conditions Extrêmes et Matériaux, Haute Température et Irradiation, 1D Avenue de la Recherche Scientifique, F-45071 Orléans Cedex 2, France*
[4]*Synchrotron-SOLEIL, L'Orme des Merisiers Saint-Aubin, BP 48, F-91192 Gif-sur-Yvette, France*
[5]*Institut des Nanosciences de Paris, UMR 7588 CNRS, Université Pierre et Marie Curie, 75252 Paris Cedex 5, France*
[6]*Laboratoire de Chimie Physique, UMR 8000, Université Paris-Sud, CNRS, Bâtiment 349, 15 rue Georges Clemenceau, F-91405 Orsay cedex, France*

(Received 18 January 2011; accepted 21 March 2011; published online 9 May 2011)

Multilayered films of Au/ZnO were prepared by physical vapor deposition. Varying the Au thickness, t_{Au}, and the number of bilayers, n, allowed us to investigate the role of these parameters on the sample structural and electronic properties. X-ray diffraction, X-ray absorption spectroscopy, grazing incidence small angle X-ray scattering and transmission electron microscopy experiments, have been combined to UV-visible and infrared spectroscopy to characterize the multilayers in the as-prepared state and after annealing. In the as-prepared state, the strong Au and ZnO lattice interaction leads to ZnO epitaxy on Au. Gold appears either as continuous layers or in form of nanoparticles. ZnO experiences a structural transformation from wurztite to rock salt monitored by the Au morphology. Annealing at 500 °C destroys the lattice matching. The electronic and optical properties of the systems are understood in line with the Au morphology and ZnO structural state. © *2011 American Institute of Physics*. [doi:10.1063/1.3580333]

I. INTRODUCTION

Heterogeneous media are good candidates for devices where the properties can be tailored versus the concentration of each constituent. Applications for these devices require a precise characterization of their final physical and chemical properties, which depend on the preparation technique and on the individual properties of each constituent. Among these media, metallic nanoparticles (NPs) embedded in oxides or in ceramics (cermets) have already shown their interesting mechanical, optical, electrical and magnetic characteristics.[1] The properties of such nanostructured materials are strongly connected to the role of interfaces, which have applications in the area of coating and wetting, for instance, and display fundamental aspects such as electronic and atomic interactions.

A way to synthesize cermets consists in applying alternate layer deposition. Depending on the individual layer thickness, one crosses the border between continuous films and particles, changing thus the dimensionality of the interface and its properties. To study such an effect keeping the other parameters constant, we have chosen sequential sputtering by physical vapor deposition (PVD) to prepare our samples. Recently, we had focused our interest on metal/Si_3N_4 multilayers showing the role of parameters such as the heat of formation of metal nitrides, the metal film thickness, t_{metal}, and the number of bilayers, n.[2] As in previous works,[3–5] these two later parameters play an important role on the transition between continuous and discontinuous layer via roughness accumulation along the growth direction.[6]

In this work, we changed the insulating nitride, Si_3N_4, to a semiconductor oxide, ZnO. In the last 5–10 years, ZnO has received interest in various fields (Ref. 7 and references therein), especially for fabricating hybrid systems of low dimensionality[8] and in the field of optoelectronics.[9] We have grown Au/ZnO multilayers with different Au thicknesses, in the 2–8 nm range, keeping the ZnO thickness between 3–4 nm, and different numbers of bilayers, from 5 to 75. Combining X-ray diffraction, X-ray absorption spectroscopy, grazing incidence small angle X-ray scattering, absorption spectroscopy in the UV-visible range, observations by transmission electron microscopy and infrared spectroscopy, we have characterized the Au/ZnO multilayers in the as-prepared and annealed state. The main results are the following: there is a strong interaction between the Au and ZnO lattices leading to epitaxial growth and flat interfaces which are destroyed only for a large number of bilayers and a small Au thickness. When Au is in form of NPs, ZnO adopts a rock salt crystallographic structure. Annealing in the conditions used here allows partial or total decoupling of the Au and ZnO lattices depending on the Au thickness with Au NPs formation. The ZnO structural state and Au morphology

a)Author to whom correspondence should be addressed. Electronic mail: agnes.traverse@u-psud.fr.

 © 2011 American Institute of Physics

Downloaded 03 May 2013 to 150.244.101.204. This article is copyrighted as indicated in the abstract. Reuse of AIP content is subject to the terms at: http://jap.aip.org/about/rights_and_permissions

TABLE I. Characteristics of the prepared ZnO[$Au_{(tAu)}$/ZnO] samples with the bilayer thickness determined by XRR (Λ_{XRR}) and by RBS (Λ_{RBS}), the number of Au atoms per layer, the Au layer thickness, the total number of Zn atoms and the ZnO thickness determined by RBS.

Sample ZnO[$Au_{(tAu)}$/ZnO]$_n$	Λ_{XRR} (nm)	Λ_{RBS} (nm) (±0.6 nm)	RBS Au atoms per layer × 10^{16} (at./cm^2) (±0.15)	RBS t_{Au} (nm) (± 0.3) (nm)	RBS Zn atoms (at./cm^2) (±0.15)	RBS t_{ZnO} (nm) (± 0.3) (nm)	Sample total effective thickness (nm)
ZnO[$Au_{(7.8)}$/ZnO]$_5$	10.5 ± 0.5	11.1	4.60	7.8	6.1×10^{16}	3.3	59
ZnO[$Au_{(4.6)}$/ZnO]$_{10}$	7.5 ± 0.5	7.6	2.71	4.6	1.0×10^{17}	3.0	79
ZnO[$Au_{(3.6)}$/ZnO]$_{20}$	6.0 ± 0.5	6.2	2.12	3.6	4.4×10^{17}	2.6	127
ZnO[$Au_{(2.4)}$/ZnO]$_{40}$	5.0 ± 0.7	5.8	1.41	2.4	1.1×10^{18}	3.4	235
ZnO[$Au_{(1.8)}$/ZnO]$_{75}$	5.0 ± 0.7	5.8	1.06	1.8	2.5×10^{18}	4.0	439

allow understanding the measured electronic and optical properties.

II. EXPERIMENTAL DETAILS

Au/ZnO multilayered films were prepared by sequential sputtering of ZnO and Au on Si(100) and quartz substrates at room temperature. The residual pressure was near 1×10^{-7} mbar. The ZnO layers were deposited by reactive sputtering from a pure Zn target (Goodfellow: 99.9%) using an O_2/Ar mixture gas (30% O_2-rich) at a working pressure of 5.4×10^{-3} mbar and a DC power of ~5.5 W. The Au layers were grown from a gold target (99.999%) at a 5.0×10^{-3} mbar pressure of pure Ar and a DC power of ~10 W. Pre-sputtering was developed before multilayer growth and also between two consecutive layers. The sequence of deposition always started and finished with a ZnO layer so as Au grew always on the same type of surface.

A series of five Au/ZnO samples, labeled as ZnO [$Au_{(tAu)}$/ZnO]$_n$ in Table I was prepared. The ZnO sputtering time per layer was maintained constant in every sample to reach a ZnO layer thickness, t_{ZnO}, approximately constant, around 3 nm. The Au layer sputtering time was varied so that the Au layer thickness (t_{Au}) ranges from about 2 to 8 nm. The number of bilayers (n) was increased for small t_{Au} in order to maintain the Au total amount sufficient for all characterization techniques to provide reliable information. In order to follow their thermal stability, two samples, labeled ann.−ZnO[$Au_{(tAu)}$/ZnO]$_n$, have been annealed at 500 °C after deposition in a vacuum system furnace, firstly evacuated up to 1×10^{-6} mbar. The thermal treatment was performed under O_2 atmosphere of 1×10^{-2} mbar for 2 hs. A pure ZnO film (110 nm thick) was also deposited on a Si(100) substrate for comparison.

To measure the multilayer period (the bilayer thickness Λ), low angle X-ray reflectometry (XRR) measurements were carried out on a Bruker D8 X-ray diffractometer with a Cu K_α source ($\lambda = 0.154$ nm). Rutherford backscattering spectrometry (RBS) was done using a 1.2 MeV He^+ beam[10] in order to get the number of Au and Zn atoms per layer. The experimental spectra were simulated by using the RBX code.[11]

Extended X-Ray absorption fine structure (EXAFS) on as-prepared multilayers were carried out at the Au L_{III}-edge in fluorescence detection mode at room temperature on the SAMBA beamline[12] at Synchrotron-SOLEIL to characterize the atomic surrounding of the Au atoms. The incident beam impinged at an angle of 45° on the sample surface with detection at 45°. Standard analysis of the EXAFS data was performed using the Cherokee software[13] and FEFF phase and amplitude.[14] The morphology of the Au layers was determined by grazing incidence small angle X-ray scattering (GISAXS) carried out on the SWING beamline at Synchrotron-SOLEIL. The wavelength of the incident X-ray beam was set at $\lambda = 0.161$ nm, the angle of incidence ($\theta_i = 0.5°$) was slightly higher than the critical angle for total reflection, θ_c, in order to achieve good surface sensitivity, and the sample-to-detector distance was 2 m. The transmitted and specularly reflected beams were masked by a vertical beam-stop and the scattered intensity was collected with a 2 D CCD detector. The experimental data were analyzed with the FitGISAXS package developed within the IGOR Pro analysis software (WaveMetrics, Inc.).[15]

Infrared (IR) spectroscopy was performed in reflection mode under an incidence of 30°, in the 60–4000 cm^{-1} range with a Bruker Vertex 70 interferometer. The measurements were made with an instrumental resolution of 4 cm^{-1} with a gold mirror as a reference. In order to extract structural information, reflectance spectra were fitted using the FOCUS code.[16]

X-ray diffraction (XRD) was carried out in a standard laboratory diffractometer (Bruker D8 TT) by using the K_α radiation line of Cu in the θ-2θ configuration.

The optical absorption of the samples grown on quartz substrates was measured in transmission mode with a Cary 4000 UV-vis spectrophotometer in the 200–900 nm range.

Transmission electron microscopy (TEM) observations were undertaken using a JEOL2000FX microscope operated at 200 kV. Samples were prepared in cross-section view by grinding and ion beam milling.

Depending on the characterization techniques carried out in reflection geometry, the probed sample depths are different. For RBS, the fact that the Si substrate is detected ensures that the whole multilayer is probed. When incident beams are X-rays in the energy range of 7–12 keV, as for EXAFS, XRD, and GISAXS experiments, the incident path is a few microns. The fluorescence detection mode used for EXAFS allows one to probe the whole sample thickness. For XRD and GISAXS, the probed depth depends on the incident beam angle, θ_i. Typically, the probed depth is in the range of a few tenth of nm for $\theta_i = 0.5°$ and of a few microns for

Downloaded 03 May 2013 to 150.244.101.204. This article is copyrighted as indicated in the abstract. Reuse of AIP content is subject to the terms at: http://jap.aip.org/about/rights_and_permissions

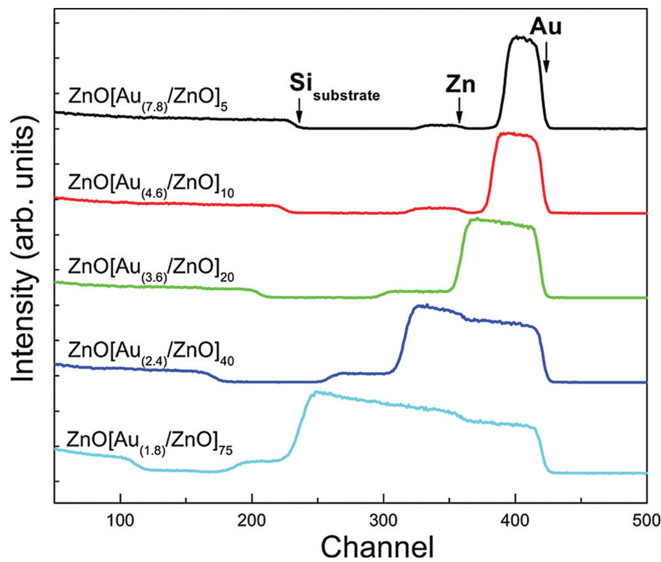

FIG. 1. (Color online) RBS spectra for the as-prepared Au/ZnO samples.

$\theta_i > 10°$. Thus, the whole sample thickness is analyzed by XRD whereas GISAXS is sensitive to the upper part of the multilayers only.

III. RESULTS

A. Rutherford backscattering spectrometry, X-Ray reflectometry and transmission electron microscopy: Multilayer characterization

RBS spectra for the as-deposited Au/ZnO samples are shown in Fig. 1. Fitting the spectra provides the number of Au atoms per Au layer, the number of Zn atoms per ZnO layer and their corresponding layer thicknesses calculated considering the Au metal bulk density ($\rho_{Au} = 5.9 \times 10^{22}$ at./cm^3) and ZnO bulk density ($\rho_{ZnO} = 8.3 \times 10^{22}$ at/cm^3) (Table I).

XRR curves for the as-deposited samples are plotted in Fig. 2(a). Several satellite maxima corresponding to heterostructure periodicity and Kiessig fringes can be observed for ZnO[$Au_{(7.8)}$/ZnO]$_5$, ZnO[$Au_{(4.6)}$/ZnO]$_{10}$ and ZnO[$Au_{(3.6)}$/ZnO]$_{20}$ showing that these multilayers are actually formed by alternate ZnO and Au-rich regions. On the contrary, only one maximum is detected for ZnO[$Au_{(2.4)}$/ZnO]$_{40}$ and ZnO[$Au_{(1.8)}$/ZnO]$_{75}$. This suggests two different behaviors depending on the Au thickness. For $t_{Au} > 3.6$ nm, sharp Au/ZnO interfaces build whereas for $t_{Au} < 2.4$ nm, out-of-plane periodicity gets bad. The bilayer thicknesses, Λ_{XRR}, obtained from the slope of m versus $\sin\theta_m$, independently of the critical angle θ_c, using the formula

$$m\lambda = 2\Lambda_{XRR}\left(\sin^2\theta_m - \sin^2\theta_c\right)^{1/2}$$

are shown in Table I. The estimated uncertainty on the Λ_{XRR} value is larger for the two smallest t_{Au} because only one maximum in the XRR curve is used. One notes the good agreement between Λ_{XRR} and Λ_{RBS} calculated as the sum of the Au and ZnO thicknesses deduced from RBS fit. The out-of-plane periodicity for ZnO[$Au_{(3.6)}$/ZnO]$_{20}$ and its disappearance for ZnO[$Au_{(1.8)}$/ZnO]$_{75}$ are confirmed by the TEM cross-section observations (Fig. 3). For ZnO[$Au_{(3.6)}$/ZnO]$_{20}$, in Fig. 3(a), a number of 20 repetitions of continuous ZnO layers (3.0 ± 0.5 nm) and Au layers (3.6 ± 0.5 nm) are observed. Layer thickness values and total film thickness (126 ± 3 nm) are well in agreement with Λ_{XRR} and Λ_{RBS} (Table I). For ZnO[$Au_{(1.8)}$/ZnO]$_{75}$, the columnar character of ZnO, which seems to influence the roughness enhancement with n, can be noticed in Fig. 3(b). Although projection effects and thickness gradient effects due to the cross-section preparation cannot be ruled out, the TEM images suggest that the first deposited layers are continuous, while the layers close to the surface are discontinuous (Fig. 3(c)). Finally, elongated wormlike Au NPs of 4 ± 1 nm height inside the ZnO matrix can be identified (Fig. 3(d)).

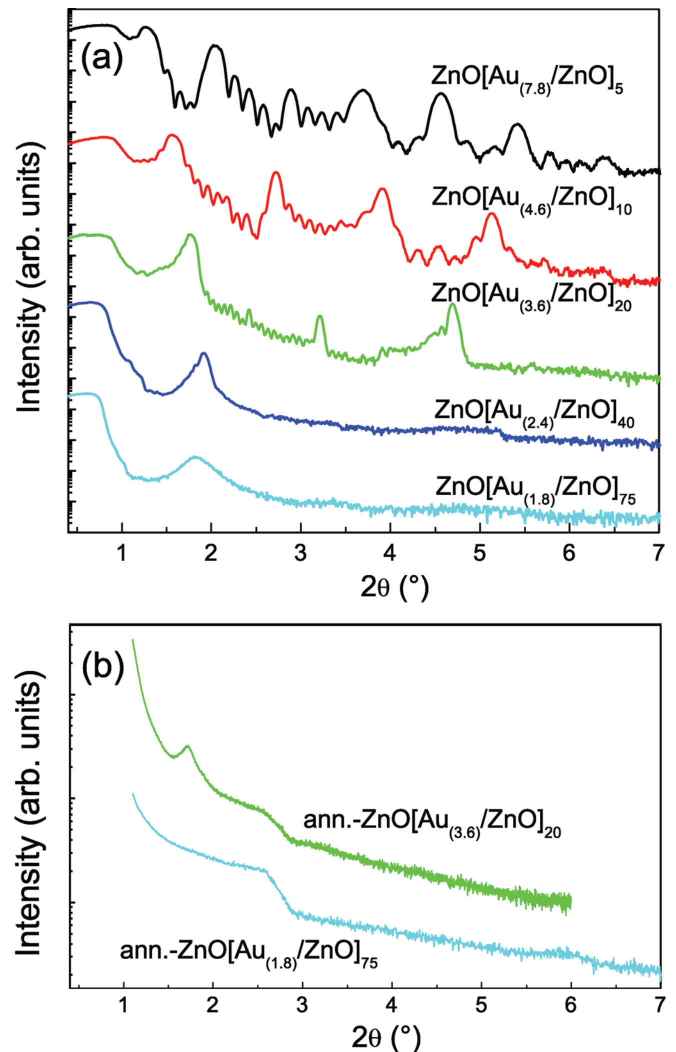

FIG. 2. (Color online) (a) X-Ray reflectometry for as deposited multilayers; (b) X-Ray reflectometry for annealed multilayers.

XRR curves for ann.-ZnO[$Au_{(3.6)}$/ZnO]$_{20}$ and ann.-ZnO[$Au_{(1.8)}$/ZnO]$_{75}$ are plotted in Fig. 2(b). The signal is strongly modified in both samples. There is a clear indication of loss of the pre-existing out-of-plane periodicity for ann.-ZnO[$Au_{(3.6)}$/ZnO]$_{20}$, for which even the Kiessig fringes, related to the total thickness, vanish. An increase of film roughness is evidenced in both annealed samples.

Downloaded 03 May 2013 to 150.244.101.204. This article is copyrighted as indicated in the abstract. Reuse of AIP content is subject to the terms at: http://jap.aip.org/about/rights_and_permissions

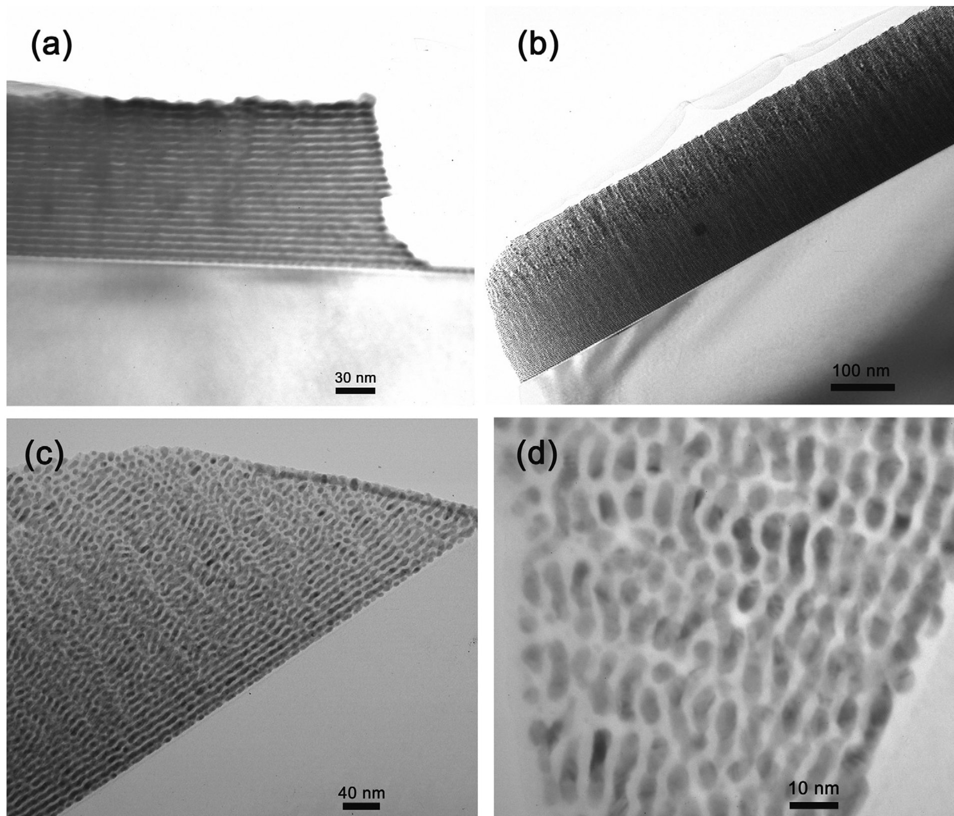

FIG. 3. TEM cross-section view for (a) $ZnO[Au_{(3.6)}/ZnO]_{20}$ and (b), (c), and (d) $ZnO[Au_{(1.8)}/ZnO]_{75}$.

B. X-ray absorption, X-ray scattering, and X-ray diffraction: Au layer structural characterization

Simulations of the experimental EXAFS provide Au-Au distances slightly smaller but in agreement with the Au metal foil reference, indicating Au metal formation in all the sample series. A significant decrease in the Au-Au coordination number N is seen when t_{Au} decreases, suggesting an evolution of the interface dimensionality between Au and ZnO.

For the $ZnO[Au_{(7.8)}/ZnO]_5$ sample, the 2 D GISAXS pattern, not shown here, is typical of a continuous layer. In contrast, for $ZnO[Au_{(2.4)}/ZnO]_{40}$ and $ZnO[Au_{(1.8)}/ZnO]_{75}$, the 2 D patterns present typical features of discontinuous Au layers. Horizontal cuts along q_y at $q_z = 1.0\ nm^{-1}$ are exhibited in Fig. 4 together with the corresponding simulated data assuming isolated spheroidal NPs with a Gaussian size distribution (mean in-plane diameter D and full width at half maximum FWHM) and an interparticle distance L. Close average diameters were measured for both samples, i.e., $D = 4.7$ and 4.1 nm, respectively (Table II). Yet, the distribution width is much larger for $ZnO[Au_{(1.8)}/ZnO]_{75}$ (2.2 nm) than for $ZnO[Au_{(2.4)}/ZnO]_{40}$ (0.9 nm). The interparticle distances are 8.2 and 4.7 nm, respectively, suggesting that the NPs present either different morphologies (i.e., the NPs in $ZnO[Au_{(2.4)}/ZnO]_{40}$ have a columnar structure) or spatial distributions (i.e., a percolated network of NPs tends to form for $ZnO[Au_{(2.4)}/ZnO]_{40}$). Let us remind that, owing to the grazing incident conditions, the probed depth corresponds to the upper part of the multilayer mainly. The detection of Au NPs for $ZnO[Au_{(1.8)}/ZnO]_{75}$ and the corresponding NPs sizes are in agreement with the TEM cross-section displayed in Fig. 3(c).

X-ray diffractograms for all samples including the ZnO film are shown in Fig. 5(a) with different vertical scales. A

TABLE II. Structural parameters determined from the analysis of the GISAXS data.[a]

Sample	D (nm)	FWHM (nm)	L (nm)
$ZnO[Au_{(2.4)}/ZnO]_{40}$	4.7	0.9	8.2
$ZnO[Au_{(1.8)}/ZnO]_{75}$	4.1	2.2	4.7

[a] D is the mean in-plane diameter of the NPs, FWHM is the full width at half maximum of the Gaussian size distribution, and L is the interparticle distance.

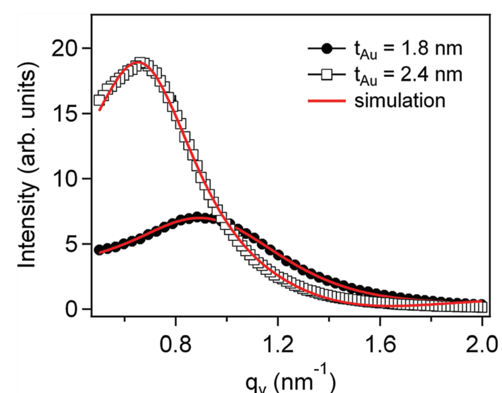

FIG. 4. (Color online) Horizontal cuts of GISAXS patterns for $ZnO[Au_{(2.4)}/ZnO]_{40}$ (open square) and $ZnO[Au_{(1.8)}/ZnO]_{75}$ (black dots).

Downloaded 03 May 2013 to 150.244.101.204. This article is copyrighted as indicated in the abstract. Reuse of AIP content is subject to the terms at: http://jap.aip.org/about/rights_and_permissions

TABLE III. Interpretation of the XRD peaks.

$ZnO[Au_{(7.8)}/ZnO]_5$	$2\theta_m$ (°)	33.50	34.71	36.23	37.40	38.22	40.20	41.54
	m	−6	−4	−2	−1	0	+2	+4
	Λ_{XRD} (nm)	11.79	10.59	9.36	11.37	—	9.46	11.31
$ZnO[Au_{(4.6)}/ZnO]_{10}$	$2\theta_m$ (°)	33.10	34.84		37.10	38.23	41.18	43.60
	m	−4	−3		−1	0	+3	+4
	Λ_{XRD} (nm)	7.23	8.22		8.25	—	9.54	7.02
$ZnO[Au_{(3.6)}/ZnO]_{20}$	$2\theta_m$ (°)		34.17		37.0	38.42	42.0	
	m		−3		−1	0	2	
	Λ_{XRD} (nm)		6.55		6.57	—	5.25	
$ZnO[Au_{(2.4)}/ZnO]_{40}$	$2\theta_m$ (°)		33.23				38.10	
	m		−3			0		
	Λ_{XRD} (nm)		5.71			—		
$ZnO[Au_{(1.8)}/ZnO]_{75}$	$2\theta_m$ (°)	33.80	35.09			38.11		
	m	—	—			0		
	Λ_{XRD} (nm)	—	—			—		
Peak attribution			W-ZnO (002)	W-ZnO (101)/RS-ZnO (111)		Au (111)		

log scale is used for $ZnO[Au_{(t)}/ZnO]_n$ on the left vertical axis and a linear scale for ZnO on the right vertical axis. The position of the observed ZnO Bragg peak in the single-layer sample is $2\theta \sim 33.7°$ smaller than the expected one at $2\theta = 34.47°$ for (002) in the wurtzite bulk structure (W-ZnO), a point which is discussed below. For the multilayers, the logarithmic vertical scale allows one to see a wide Bragg peak at $2\theta_0 \sim 38.2°$ together with satellite peaks located at $2\theta_m$ on each side of the main one. These satellite peaks are rather intense for $ZnO[Au_{(7.8)}/ZnO]_5$, faint for $ZnO[Au_{(3.6)}/ZnO]_{20}$ and $ZnO[Au_{(2.4)}/ZnO]_{40}$ and nearly absent for thinner Au layers. The two thin peaks marked with stars belong to the Si substrate. A fit of the X-ray diffractograms has been done in the 30–45° 2θ range with Gaussian contributions superimposed on a linear background, providing peak positions (Table III). An example is shown in Fig. 5(b) for $ZnO[Au_{(7.8)}/ZnO]_5$. The contribution at $2\theta_0 = 38.22°$ may be attributed to Au(111) in the fcc structure which provides a lattice parameter of 0.407 nm, close to the Au bulk one of 0.408 nm (Table III). Note that no Bragg peak at $2\theta = 44.37°$ corresponding to Au(200) expected for a polycrystalline sample is observed meaning that the Au grains are strongly oriented, in agreement with a Au crystallographic structure matching the ZnO one. Also, the presence of satellites suggests that a coherent deposition of layers takes place.[17] In such a case, the bilayer thickness, Λ_{XRD}, is written as

$$m\lambda = 2\,\Lambda_{XRD}\left(\sin^2\vartheta_m - \sin^2\vartheta_0\right),$$

where λ is the incident beam wavelength. In Table III, an interpretation of the peaks in terms of superstructures is proposed. The Λ_{XRD} values calculated for all the layered samples are presented together with the ϑ_m attribution. Note that in most cases, Λ_{XRD} compares well with Λ_{XRR} and Λ_{RBS} given in Table I, which confirms that a mixing of the Au signal with the coherent one is induced. The most coherent layered stack expected for $ZnO[Au_{(7.8)}/ZnO]_5$ gives rise to an intense peak superimposed on the Au contribution. The coherency decreases either with the number of Au layers and(or) with the Au thickness explaining the trend observed in Fig. 5(c), where the integrated intensity of the Au(111) Bragg peak plotted versus the total Au thickness, does not increase as expected. Finally, an attempt has been made to attribute the satellite peaks to ZnO under the wurtzite structure encountered for this oxide as bulk or deposited as thin film,[18] and under the rock salt (RS-ZnO)[19,20] or zinc-blende structures,[21] energetically less favored. In Table III, it can be seen that the (111) contributions of RS-ZnO together with the (101) of W-ZnO may eventually be encountered. Nevertheless, it is worth noting that the atomic ZnO arrangement cannot be determined for certain from XRD since the lattice matching induces a mixing of the Au and ZnO diffractograms.

The X-ray diffractogram for ann.$-ZnO[Au_{(1.8)}/ZnO]_{75}$ is shown in Fig. 5(d). The (002) contribution due to W-ZnO is now present, together with the (111), (200), and (220) contributions due to polycrystalline Au, meaning that annealing has induced the loss of Au and ZnO lattice matching.

C. Infrared spectroscopy: ZnO structural characterization

Fitted and experimental reflectances in the infrared range for pure ZnO, for as-prepared and annealed $ZnO[Au_{(3.6)}/ZnO]_{20}$ and $ZnO[Au_{(1.8)}/ZnO]_{75}$ are plotted in Fig. 6. Samples with $t_{Au} = 3.6$ nm display a large nearly constant reflectance which decreases from 0.95 for the as prepared state down to 0.73 after annealing. The reflectance for $ZnO[Au_{(7.8)}/ZnO]_5$, not presented here, is also close to 1 in agreement with the fact that this sample has been seen as continuous by GISAXS. A similar high reflectance is measured for $ZnO[Au_{(4.6)}/ZnO]_{10}$. The reflectance for pure ZnO is much lower with one contribution around 400 cm^{-1}. The reflectance decrease above $\omega = 200$ cm^{-1} is due to the rough rear side of the Si substrate. This effect, absent for as-prepared and annealed $ZnO[Au_{(3.6)}/ZnO]_{20}$, indicates that the incident IR beam cannot penetrate through the whole stack. The $ZnO[Au_{(1.8)}/ZnO]_{75}$ sample displays a larger reflectance than pure ZnO with supplementary features in the frequency range from 200 to 2000 cm^{-1}. After annealing, the spectrum

Downloaded 03 May 2013 to 150.244.101.204. This article is copyrighted as indicated in the abstract. Reuse of AIP content is subject to the terms at: http://jap.aip.org/about/rights_and_permissions

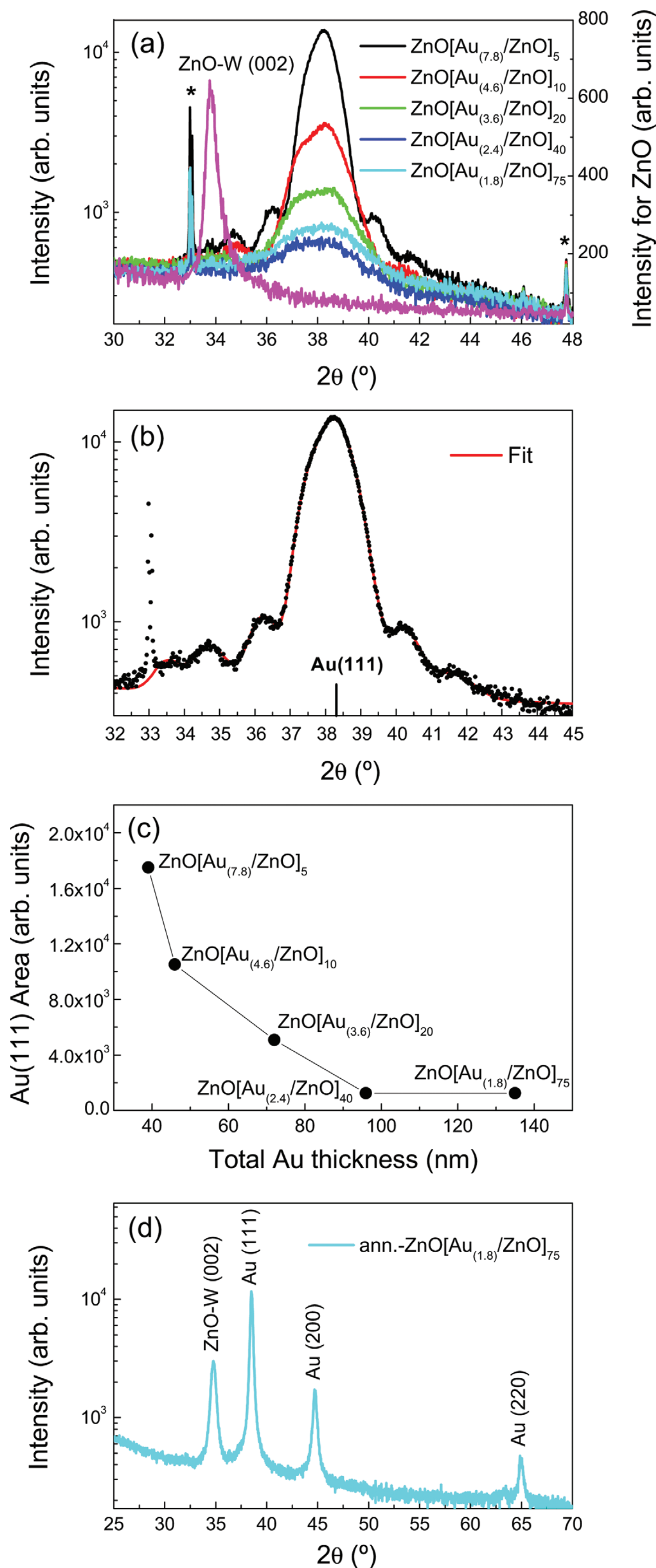

FIG. 5. (Color online) (a) X-ray diffractograms for as prepared samples and a ZnO film; note the different vertical scales: log. scale for $ZnO[Au_{(t)}/ZnO]_n$ on the left vertical axis, linear scale for ZnO on the right vertical axis; (b) X-ray diffractogram fit for $ZnO[Au_{(7.8)}/ZnO]_5$; (c) Integrated intensity of the Au(111) Bragg peak versus the total Au thickness; and (d) X-ray diffractogram for annealed $ZnO[Au_{(1.8)}/ZnO]_{75}$.

is strongly modified with a nearly uniform intensity decrease when the frequency is increased. The contribution around 400 cm^{-1} is present as in pure ZnO.

The curves have been fitted in the range 200–4000 cm^{-1} (Fig. 6). The model used for calculating the reflectance takes into account the 50%s–50%p polarization of the incident IR beam, the dielectric functions of the film, $\epsilon(\omega)$, and of the Si substrate. The latter is written as $a+ib$, where a is fixed to 12.[22] The b value is adjusted to take into account the rough rear side of the substrate in order to fit the ZnO reflectance. The dielectric function for pure ZnO and for as-prepared $ZnO[Au_{(1.8)}/ZnO]_{75}$, is written as the sum of a constant contribution due to bound electrons, ε_∞, and Gaussian components which take into account the absorption of distributions of vibrational modes occurring in disordered materials.[16,23] Each absorption band j is characterized by three parameters, A_j, ω_j, and σ_j, which represent respectively the amplitude, the peak position and the full width at half maximum. The fitting procedure also needs to introduce the film thickness, d, and substrate thickness. The substrate thickness is kept at its value of 280 μm whereas d is a free parameter. Frequency of each vibration mode, ω_j, and its intensity calculated as $(A_j)(\sigma_j)(\pi/4\ln 2)$ extracted from the fitting procedure are gathered in Table IV.

For pure ZnO, one layer 110 nm thick over Si is considered. A TO phonon-mode is seen at 395 cm^{-1} with the corresponding LO mode in agreement with values from the literature.[18,24] This value lies between the A1 (TO) mode at 380 cm^{-1} and E1 (TO) mode at 407 cm^{-1} detected by Raman measurements.[25] The contribution at 488 cm^{-1} corresponds to an exciton at 60.5 meV in agreement with the literature.[7] The ε_∞ value of 1.1 is much smaller than those of 3.5–3.8 (Ref. 24) and 2.6 (Ref. 26). Ghosh *et al.*[27] measured the dielectric functions for $Zn_{(1-x)}Ni_xO$ systems with $x=0.02$, 0.04, and 0.06, leading to an ε_∞ value of 2.2 for $x=0$.

For as-prepared $ZnO[Au_{(1.8)}/ZnO]_{75}$, several contributions have to be introduced in the dielectric function. A rather good simulation is obtained with a high ε_∞ value and a thickness smaller than the expected one by a factor of about 2. The dielectric function of the substrate is constant and equal to 21. These two last data are in line with the TEM observation where the sample appears as made of a multilayered system with continuous Au layers close to the substrate and with noncontinuous Au layers close to the air. Among the vibrational frequencies, a fundamental one at $\omega_{2i}=416$ cm^{-1} is detected corresponding to $i=1$ and its overtones at 822, 1227, and 1652 cm^{-1}, corresponding to $i=2$, $i=3$, and $i=4$, respectively. Other modes at 335, 747, 1010, and 1354 cm^{-1} have to be introduced in the fitting procedure. A contribution at 3580 cm^{-1}, not given in Table IV, but visible in the reflectance indicates presence of OH contaminations. The ε_∞ value of 18 is consistent with the presence of Au in ZnO. Such an increase has already been seen for Au in cermets.[6]

Overtones in ZnO have been calculated and their presence confirmed mainly by Raman spectroscopy.[25,28,29] The contribution at 416 cm^{-1} is close to the E1 (TO) mode, actually slightly larger, which corresponds to atoms moving perpendicular to the c axis of the wurtzite structure (Ref. 7 and references therein). Table IV shows that the intensities for these overtones are close to the one for the fundamental

Downloaded 03 May 2013 to 150.244.101.204. This article is copyrighted as indicated in the abstract. Reuse of AIP content is subject to the terms at: http://jap.aip.org/about/rights_and_permissions

TABLE IV. Parameters for the dielectric functions.[a]

ZnO	ε_∞	ω_1 (cm^{-1})		ω_2 (cm^{-1})			d (nm)
	1.1	395		488			110
ZnO[$Au_{(1.8)}$/ZnO]$_{75}$	ε_∞	ω_1 (cm^{-1})	intensity	ω_{2i} (cm^{-1})	intensity		
	18	335	12320	i = 1 416	1140		240
		747 = 335 + 416		i = 2 822	990		
		1010 = 2*335 + 416		i = 3 1247	1500		
		1354 = 3*335 + 416		i = 4 1652	970		
ann.-ZnO[$Au_{(1.8)}$/ZnO]$_{75}$	ε_∞	ω_1 (cm^{-1})		ω_p (cm^{-1})	ω_p (eV)	γ (cm^{-1})	
	18	400		89000	11	882	100
ZnO[$Au_{(3.6)}$/ZnO]$_{20}$	ε_∞			ω_p (cm^{-1})	ω_p (eV)	γ (cm^{-1})	
ann.-ZnO[$Au_{(3.6)}$/ZnO]$_{20}$	0			73000	9	1600	35
	0			73000	9	8500	24

[a]ε_∞, ω_j and intensity of the vibration modes for the overtones; plasmon energy, ω_p, and scattering time, γ, for the electronic contributions together with the sample thickness, d.

mode at 416 cm^{-1}. A very similar evolution versus the ordinal number are reported in Raman measurements on ZnO particles with diameters of 4–5 nm close to the ZnO layer thickness in our multilayers.[29]

The frequency detected at 335 cm^{-1} is much lower than the A1 (TO) mode reported at 380 cm^{-1}. Note that a frequency of 332 cm^{-1} was detected by Raman spectroscopy corresponding to the difference between the E2-low and E2-high modes,[28] yet these modes are not IR active. This frequency is either related to Au-O vibrations or to distorted ZnO layers in contact with Au ones. In the literature, vibrational frequencies are calculated at 580 cm^{-1} and 563 cm^{-1} for Au_2O_3 and Au_2O, respectively,[30] which allows us to reject this attribution. Serrano *et al.*[31] calculated the phonon modes for the different structural states of ZnO including rock salt (RS) and zinc blende (ZB). A TO mode is found for RS-ZnO at 353 cm^{-1}, closer to our experimental value. Moreover, Bundesman *et al.*[32] applied IR spectroscopic ellipsometry to $Mg_xZn_{1-x}O$ films displaying a RS structure for $x > 0.67$.

Extrapolation of the measured TO mode frequency to $x = 0$ leads to a value of 300 cm^{-1}. It is thus tempting to attribute this mode detected here at 335 cm^{-1} to RS-ZnO. The contributions at 747, 1010, and 1354 cm^{-1} could be seen as the multi-phonon combinations of $(416 + ix335)$ cm^{-1} with

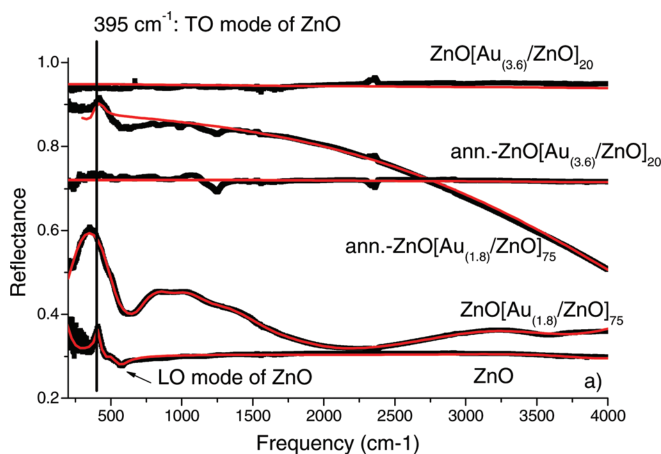

FIG. 6. (Color online) Experimental and fitted IR spectra for pure ZnO and for as prepared and annealed ZnO[$Au_{(3.6)}$/ZnO]$_{20}$ and ZnO[$Au_{(1.8)}$/ZnO]$_{75}$.

$i = 1$, 2, and 3, respectively. One notes that the intensity of the mode at 335 cm^{-1} is 10 times higher than the one at 416 cm^{-1} (Table IV). According to this discussion, we suggest an interpretation in line with the TEM cross section picture of this sample. The multilayer is divided in two parts, an upper thick part close to the surface where Au NPs are embedded in ZnO, a thinner part below where the ZnO planes are in contact with Au ones. In the upper part, ZnO is strongly deformed and adopt a rock salt lattice giving rise to a vibrational main frequency at 335 cm^{-1}. In the lower part, which contains continuous Au and ZnO layers, ZnO is in the wurtzite in-plane compressed state.

For ann-.ZnO[$Au_{(1.8)}$/ZnO]$_{75}$, the high reflectance value is an indication of the metallic character of the sample which nevertheless, has kept a ZnO vibrational contribution around 400 cm^{-1}. The dielectric function is thus written as the sum of ε_∞ and Gaussian components plus a Drude component, ϵ_D, written as

$$\varepsilon_D = -\omega_p^2/\left(\omega^2 + i\omega\gamma\right),$$

where ω_p is a plasma frequency related to the number of free electrons and γ is a scattering time.[23] The vibrational frequency and the ε_∞ value remain close to the one of ZnO[$Au_{(1.8)}$/ZnO]$_{75}$, i.e., 400 cm^{-1} and 18, respectively. The plasmon energy of 11 eV is larger than the one of pure Au, 9 eV.[33,34] Note that the thickness is much smaller than for ZnO[$Au_{(1.8)}$/ZnO]$_{75}$. Yet a faint vibrational contribution around 1100 cm^{-1} can be attributed to Si-O bonds, i.e., Si oxidation resulting from the thermal treatment. This looks contradictory with the smaller thickness evaluation discussed above. To overcome this contradiction, one must think of a rather inhomogeneous sample at a macroscopic scale with a discontinuous Au layer offering the possibility that part of the IR incident beam reaches the substrate-sample interface where the oxidized Si layer has formed.

For the as-prepared and annealed ZnO[$Au_{(3.6)}$/ZnO]$_{20}$, the high reflectance values, nearly constant versus ω, are consistent with a metallic character. The dielectric function is thus written as $\varepsilon_\infty + \epsilon_D$. Fitted spectra are presented in Fig. 6 and extracted d, ω_p, and γ are gathered in Table IV. Note that it is possible to obtain reasonable fits with ω_p values of pure Au, 9 eV, in line with the existence of a thick Au

Downloaded 03 May 2013 to 150.244.101.204. This article is copyrighted as indicated in the abstract. Reuse of AIP content is subject to the terms at: http://jap.aip.org/about/rights_and_permissions

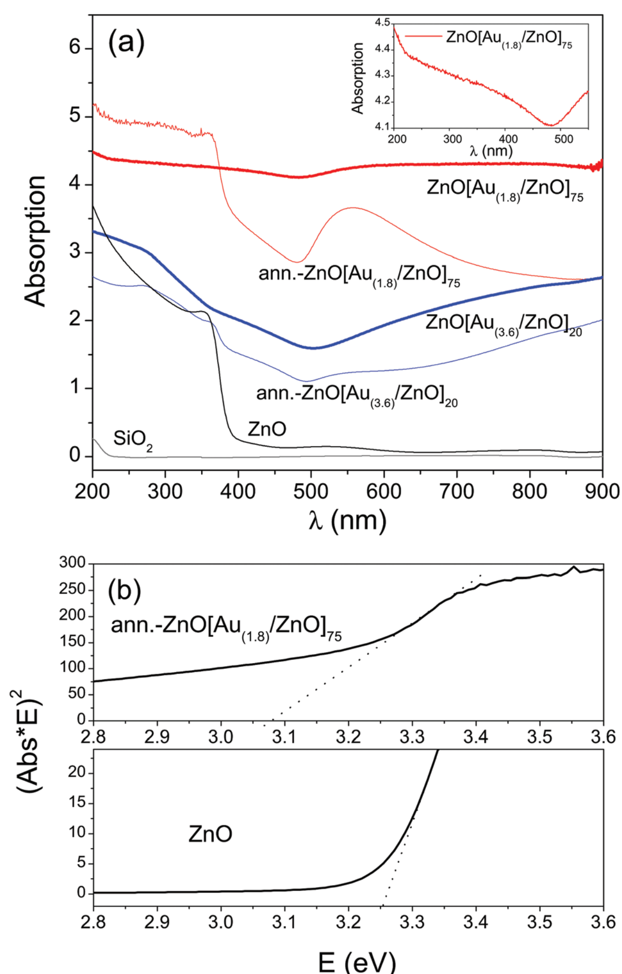

FIG. 7. (Color online) (a) Optical responses for $ZnO[Au_{(3.6)}/ZnO]_{20}$ and $ZnO[Au_{(1.8)}/ZnO]_{75}$ as prepared and after annealing, for pure ZnO and fused silica. Inset: absorption for $ZnO[Au_{(1.8)}/ZnO]_{75}$ in the 250–500 nm range, (b) Tauc plots for pure ZnO and ann.-$ZnO[Au_{(1.8)}/ZnO]_{75}$.

layer.[33,34] The thicknesses are much smaller than the total ones and are close to 4–5 times the sum of $t_{Au} + t_{ZnO}$, the thickness of $ZnO[Au_{(3.6)}/ZnO]_{20}$ being necessarily larger than the one of ann.$-ZnO[Au_{(3.6)}/ZnO]_{20}$. The γ term is larger for ann.$-ZnO[Au_{(3.6)}/ZnO]_{20}$ than for $ZnO[Au_{(3.6)}/ZnO]_{20}$. The vibrational contribution around 1100 cm^{-1} attributed to Si-O bonds is visible in ann.$-ZnO[Au_{(3.6)}/ZnO]_{20}$ and not detected in $ZnO[Au_{(3.6)}/ZnO]_{20}$. A similar interpretation as given for ann.-$ZnO[Au_{(1.8)}/ZnO]_{75}$, is suggested, the Au layer being discontinuous which could explain the larger γ term.

D. Visible spectroscopy: Au and ZnO electronic characterization

The optical responses in the visible wavelength (λ) range for $ZnO[Au_{(3.2)}/ZnO]_{20}$, $ZnO[Au_{(1.8)}/ZnO]_{75}$, and the same samples after annealing are compared to those of the ZnO film and transparent amorphous quartz substrate in Fig. 7(a). The signal of the substrate is negligible as compared to the one of the other samples.

The ZnO film displays an edge close to 380 nm and a faint contribution between 500 and 600 nm. The faint signal could be correlated to oxygen vacancies[35] although effect of interferences due to sample thickness (110 nm) is not excluded in this range. To deduce the optical bandgap, the Tauc relationship is often used

$$\alpha h\nu = A(h\nu - Eg)^n,$$

where α is the absorption coefficient, A is a constant, h Planck's constant, ν the photon frequency, E_g the optical bandgap, and n is $1/2$ for direct bandgap semiconductors.

We determined a bandgap energy of the ZnO film of 3.25 eV (Fig. 7b) close to 3.236 eV for ZnO particles[36] and not far from the bulk one of 3.4 eV (Ref. 7 and references therein).

When stacked with Au layers, in the as-prepared samples, the optical response is modified. The absorbance is higher due to the Au presence. For $ZnO[Au_{(1.8)}/ZnO]_{75}$, the ZnO absorption edge with a steplike feature is no longer detected, as seen in the inset of Fig. 7(a). IR spectroscopy indicates a RS-ZnO atomic arrangement on top of this sample. RS-ZnO is an indirect semiconductor with a bandgap in the 2.45-2.8 eV range[19,20] with an absorption edge displaying a $(1/\lambda)^2$ dependence.[19,20] The absorption versus λ observed in the range 250–400 nm for $ZnO[Au_{(1.8)}/ZnO]_{75}$ is close to a $(1/\lambda)^2$ dependence.

The behavior of as-deposited $ZnO[Au_{(3.6)}/ZnO]_{20}$ is close to its annealed state discussed below. The absorption for the annealed samples can be shared in three wavelength ranges. Between 200 and 400 nm, the ZnO edge is visible again, corresponding to an optical bandgap of 3.07 eV (Fig. 7(b)) for ann.-$ZnO[Au_{(1.8)}/ZnO]_{75}$ and too faint to get a reliable value for ann.- $ZnO[Au_{(3.6)}/ZnO]_{20}$. Above 500 nm, ann.-$ZnO[Au_{(1.8)}/ZnO]_{75}$ exhibits a well defined surface plasmon resonance at 555 nm, as measured for Au in ZnO prepared by spin coating metal-ion doped solutions of zinc acetylacetonate heated to 400 °C (Ref. 37). A very small plasmon at 550 nm is seen for ann.-$ZnO[Au_{(3.6)}/ZnO]_{20}$ followed by a signal which can be due to the contribution of percolated Au NPs. Between 400 and 500 nm, a tail is present in both samples. In thin ZnO films, such a tail, called Urbach tail, has been attributed to structural disorder.[38] XRD shows a W-ZnO(002) contribution at 34.69° for both annealed samples, less stressed than the as prepared film. This zone also corresponds to interband transitions in bulk Au.[33] An interpretation of this zone is more likely related to interband transitions in large Au NPs.

IV. DISCUSSION

Considering the ZnO growth on Si, the single-layer sample shows the (002) diffraction peak of W-ZnO,[39] evidencing a textured film with wurtzite crystallographic structure. Similar growth was found on other substrates, sapphire (11–20), silica glass and lime glass.[40] The displacement of the Bragg peak toward lower angle was already observed in sputtered ZnO films of similar thickness prepared under different conditions, as well as in $Zn_{0.95}Mn_{0.05}O$ films.[41] These studies indicate the presence of tensile stresses in the direction perpendicular to the substrate in the as-grown films, both ZnO

Downloaded 03 May 2013 to 150.244.101.204. This article is copyrighted as indicated in the abstract. Reuse of AIP content is subject to the terms at: http://jap.aip.org/about/rights_and_permissions

and $Zn_{0.95}Mn_{0.05}O$. Annealing in oxygen atmosphere improves crystallinity and leads to stress relaxation, shifting the (002) peak position to 34.4°, the stress-free powder value. As-deposited ZnO films appear elastic enough to support large stresses. IR and UV-vis. spectroscopies also detected the wurtzite phase with a vibrational contribution, a direct bandgap and an exciton binding energy in agreement with the literature. The ε_∞ value is the only one smaller than those encountered in the literature, which could be due to the lower film density as compared to the bulk one.

For the as-deposited ZnO/Au multilayers, two main results should be underlined: (1) the morphology of the Au layers is either continuous or in form of NPs, (2) the ZnO atomic arrangement is either wurtzite or rock salt. Before addressing the electronic properties of the stacks, the discussion is organized along these two points. For $t_{Au} = 7.8$ nm, the Au layers are continuous with a unique (111) orientation. It is still true when t_{Au} is decreased to 3.6 nm for n up to 20. It is only for thinner Au layers that the number of bilayers combined with the Au thickness plays a role on the Au layer morphology. For $t_{Au} = 1.8$ nm for example, provided $n \leq 20$–25, the layers are continuous whereas for larger n the upper part of the multilayer is made of connected NPs, as a result of roughness accumulation and columnar ZnO growth. In Au/Si_3N_4 stacks with a Si_3N_4 thickness similar to the one of ZnO, the transition from continuous Au to Au NPs is observed provided $t_{Au} = 3$ nm.[6] Note also that for $t_{Au} = 1.6$ nm, the diameter D of Au NPs is about 6.5 nm when embedded in Si_3N_4 whereas for $t_{Au} = 1.8$ nm, D is about 4 nm when embedded in ZnO. The key is in the elastic properties of the matrix and its possible structural modification: (1) Si_3N_4 is not as elastic as ZnO, (2) it is amorphous in the as-deposited state and crystallizes under Au deposition,[6] whereas ZnO is already in a crystalline state. To enlighten this point, we discuss the ZnO atomic arrangement.

Whatever t_{Au} in the range studied here, for the as-grown $ZnO[Au_{(t)}/ZnO]_n$ multilayers, there is a strong lattice interaction between Au and ZnO. Gold always grows with a (111) orientation as seen by XRD. The ZnO lattice experiences a deformation so that its crystallographic structure matches the Au one. Two different situations have to be distinguished. When Au continuous layers are formed, ZnO adopts a wurtzite stressed structure. When Au forms NPs, ZnO adopts a rock salt structure. IR spectroscopy thanks to the phonon contributions, either at 395 cm^{-1} for W-ZnO or at 335 cm^{-1} for RS-ZnO, brings here a useful insight. The question is the driving force leading to this structural modification. Stacking of ZnO with Ag, another fcc metal, shows no wurtzite to rock salt transition. Kato *et al*. found (111)-oriented Ag layers, 10 nm thick, on wurtzite (001)-oriented ZnO layers, 37 nm thick, grown by magnetron sputtering.[42] Sahu *et al*.[43] using the same preparation technique found polycrystalline ZnO and Ag for Ag thickness >4 nm and ZnO thickness of 20 nm. Yet the thickness of ZnO is larger in these samples than in ours. RS-ZnO has been observed from W-ZnO under pressure,[20] by Zn and O co-implantation in MgO (Ref. 19) or by deposition on MgO (Ref. 44). The lattice parameter of RS-ZnO is about 0.42 nm (Ref. 7 and references therein). The lattice mismatch with Au is then only about 3%. The driving force for the structural transition could be the reduction of stress. The structural transition occurs (1) when part of the ZnO lattice is located in between the Au NPs, thus it is strongly related to the Au morphology change from continuous to NPs, (2) provided the ZnO thickness is not too large. Changing the deposition parameters during the multilayer fabrication, gas pressure and sputtering power, could increase the layer roughness, favoring Au NPs formation at lower n values and consequently the RS-ZnO formation. Varying the oxide layer thickness could also play a role since, as seen in Ref. 42 and 43, thick W-ZnO are stable and does not experience a lattice modification.

After annealing in oxygen, increase of crystalline grain size and stress relaxation promote the loss of the lattice matching. In agreement, the W-ZnO peak appears for ann.-$ZnO[Au_{(1.8)}/ZnO]_{75}$, associated with the vibrational contribution at 400 cm^{-1}, still with Au (111) preferential growth. This result suggests that increasing substrate temperature during deposition can influence the Au and ZnO lattice coupling eventually preventing from RS-ZnO formation.

Electronic properties are detected via the IR and UV-vis. spectra. For as-deposited $ZnO[Au_{(3.6)}/ZnO]_{20}$, the multilayer displays large IR reflectance and absorption in the UV-vis. wavelength range in agreement with its high metallic character due to the Au continuous layers. There is still a faint semiconducting behavior, the gap being coherent with W-ZnO. Annealing of this sample modifies neither its behavior as seen by IR and UV-vis. spectroscopy, nor its structural properties. For as-deposited $ZnO[Au_{(1.8)}/ZnO]_{75}$, IR spectroscopy detects a partially transparent stack whereas UV-vis. spectroscopy detects another semiconducting behavior with a totally modified gap. An interpretation is given in line with the presence of Au NPs close to the top of the stack and consequently a transition from W-ZnO to RS-ZnO. After annealing, the bandgap of W-ZnO is detected together with the plasmon resonance of Au NPs providing a mixed semiconducting-metallic system.

V. CONCLUSION

The atomic arrangement of ZnO and the Au morphology has been studied in $ZnO[Au_{(t)}/ZnO]_n$ multilayers prepared by sequential sputtering at room temperature with 1.8 nm $\leq t_{Au} \leq 7$ nm and $5 \leq n \leq 75$, the ZnO thickness being kept around 3 nm. In the deposition conditions used here, there is a strong matching of the ZnO lattice to the Au one, thanks to the elastic properties of this oxide. The main result is that the ZnO layers experience a structural change from W-ZnO to RS-ZnO when Au changes its morphology from continuous to NPs. It could be a way to monitor the ZnO atomic arrangement. The electronic properties studied via IR and UV-vis. spectroscopies are interpreted in terms of W-ZnO to RS-ZnO transition and Au morphology.

Because of lattice matching of ZnO on Au, XRD could not detect the structure of ZnO. We underline the original exploitation of IR spectroscopy which, thanks to the phonon contributions, at 395 cm^{-1} for W-ZnO and at 335 cm^{-1} for RS-ZnO, brings here a useful insight on the atomic arrangement.

Downloaded 03 May 2013 to 150.244.101.204. This article is copyrighted as indicated in the abstract. Reuse of AIP content is subject to the terms at: http://jap.aip.org/about/rights_and_permissions

ACKNOWLEDGMENTS

This work has been partially supported under Spanish MICINN contract MAT2009-08786. We also thank the TEM service of the ICMM and Sonia Molina for the support in the cross- sections preparation.

[1]J. S. Moya, S. Lopez-Esteban, and C. Pecharromán, Prog. Mater. Sci. **52**, 1017 (2007).
[2]E. Céspedes, D. Babonneau, O. Lyon, J. Sanchez-Marcos, R. Stephan, C. Prieto, O. Luca, and A. Traverse, J. Appl. Phys. **107**, 104306 (2010).
[3]A. P. Payne and B. M. Clemens, Phys. Rev. B **47**, 2289 (1993).
[4]V. P. Romanov, S.V. Ulyanov, V. M. Uzdin, G. Nowak, M. Vadala, and H. Zabel, J. Phys. D: Appl. Phys. **41**, 115401 (2008).
[5]S. P. Vernon, D. G. Stearns, and R. S. Rosen, Appl. Optics **32**, 6969 (1993).
[6]E. Céspedes, J. Toudert, D. de Sousa Meneses, C. Prieto, and A. Traverse, J. Appl. Phys. **108**, 124309 (2010).
[7]Ü. Özgür, Y. I. Alivov, C. Liu, A. Teke, M. A. Reshchikov, S. Doğan, V. Avrutin, S.-J. Cho, and H. Morkoç, J. Appl. Phys. **98**, 041301 (2005).
[8]X. Han, W.-J. Qin, J. Sun, J. Yang, K.-Y. Niu, H.-L. Wang, and X.-W. Du, Mater. Lett. **63**, 1093 (2009).
[9]E. Millon, J. Perrière, S. Tricot, and C. Boulmer-Leborgne, Proc. SPIE, **7005**, 70051A (2008).
[10]SAFIR, available at www.insp.jussieu.fr/safir/.
[11]E. Kotai, Nucl. Instrum. Methods B **85**, 588 (1994).
[12]SAMBA, available at www.synchrotron-soleil.fr.
[13]Outils et méthodes pour l'analyse des spectres EXAFS, rubrique 340, available at www.icmpe.cnrs.fr/spip.php.
[14]S. I. Zabinsky and J. J. Rehr, Phys. Rev. B **52**, 2995 (1995).
[15]D. Babonneau, J. Appl. Crystallogr. **43**, 929 (2010).
[16]D. de Sousa Meneses, J. F. Brun, P. Echegut, and P. Simon, Appl. Spectrosc. **58**, 969 (2004).
[17]E. E. Fullerton, I. K. Schuller, H. Vanderstraeten, and Y. Bruynseraede, Phys. Rev. B **45**, 9292 (1992).
[18]D. C. Agarwal, F. Singh, D. Kabiraj, S. Sen, P. K. Kulariya, I. Sulania, S. Nozaki, R. S. Chauhan, and D. K. Avasthi, J. Phys. D.: Appl. Phys. **41**, 045305 (2008).
[19]S. W. H. Eijt, J. de Roode, H. Schut, B. J. Kooi, and J. T. M. De Hosson, Appl. Phys. Lett. **91**, 201906 (2007).
[20]A. Segura, J. A. Sans, F. J. Manjón, A. Muñoz, and M. J. Herrera-Cabrera, Appl. Phys. Lett. **83**, 278 (2003).
[21]A. Ashrafi and C. Jagadish, J. Appl. Phys. **102**, 071101 (2007).
[22]E. D. Palik, *Handbook of Optical Constants III* (Academic, New York, 1998).
[23]R. E. Kroon, Infrared Phys. Techn. **51**, 31 (2007).
[24]C. Bundesmann, N. Ashkenov, M. Schubert, A. Rahm, H. V. Wenckstern, E. M. Kaidashev, M. Lorenz, and M. Grundmann, Thin Solid Films **455-456**, 161 (2004).
[25]T. C. Damen, S. P. S. Porto, and B. Tell, Phys. Rev. **142**, 570 (1966).
[26]G. E. Jellison and L. A. Boatner, Phys. Rev. B **58**, 3586 (1998).
[27]C. K. Ghosh, S. Malkhandi, M. K. Mitra, and K. K. Chattopadhyay, J. Phys. D: Appl. Phys. **41**, 245113 (2008).
[28]H. W. Kunert, D. J. Brink, F. D. Auret, J. Malherbe, J. Barnas, and V. Kononenko, Phys. Stat. Sol. C **2**, 1131 (2005).
[29]X. Wang, X. Kong, Y. Yu, and H. Zhang, J. Phys. Chem. C **111**, 3836 (2007).
[30]H. Shi, R. Asahi, and C. Stampfl, Phys. Rev. B **75**, 205125 (2007).
[31]J. Serrano, A. H. Romero, F. J. Manjón, R. Lauck, M. Cardona, and A. Rubio, Phys. Rev. B **69**, 094306 (2004).
[32]C. Bundesman, A. Rahm, M. Lorenz, M. Grundmann, and M. Shubert, J. Appl. Phys. **99**, 113504 (2006).
[33]P. G. Etchegoin, E. C. Le Ru, and M. Meyer, J. Chem. Phys. **125**, 164705 (2006).
[34]P. B. Johnson and R. W. Christy, Phys. Rev. B **6**, 4370 (1972).
[35]H. Seo, C.-J. Park, Y.-J. Cho, Y.-B. Kim, and D.-K. Choi, Appl. Phys. Lett. **96**, 232101 (2010).
[36]P. Singh, A. Kumar, A. Kaushal, D. Kaur, A. Pandey, and R. N. Goyal, Bull. Mater. Sci. **31**, 573 (2008).
[37]B. J. Bozlee and G. J. Exarhos, Thin Solid Films **377-378**, 1 (2000).
[38]D. Dimova-Malinovska, H. Nichev, and O. Angelov, Phys. Stat. Sol. **5**, 3353 (2008).
[39]E. Céspedes, J. Sánchez-Marcos, J. Garcia-López, and C. Prieto, J. Magn. Magn. Mater. **322**, 1201 (2010).
[40]C. Huang, M. Wang, Y. Cao, Q. Liu, Z. Huang, Y. Li, W. Guo, and Q. Huang, J. Phys. D: Appl. Phys. **42**, 165306 (2009).
[41]E. Céspedes, R. J. Jiménez-Riobóo, M. Vila, and C. Prieto, Supperlattice Microst. **39**, 75 (2006).
[42]K. Kato, H. Omoto, and A. Takamatsu, Vacuum **83**, 606 (2009).
[43]D. R. Sahu, S.-Y. Lin, and J.-L. Huang, Appl. Surf. Sci. **515**, 7509 (2006).
[44]H. T. Yuan, Y. Z. Liu, Z. X. Mei, Z. Q. Zeng, Y. Guo, X. L. Du, J. F. Jia, Z. Zhang, and Q. K. Xue, J. Cryst. Growth **312**, 263 (2010).

Downloaded 03 May 2013 to 150.244.101.204. This article is copyrighted as indicated in the abstract. Reuse of AIP content is subject to the terms at: http://jap.aip.org/about/rights_and_permissions